mathematics

MDPI

Article

Damage and Failure Modeling of Composite Material Structures Using the Pam-Crash Code

Eduardo Martin-Santos [1,2,*], Lucia G. Barbu [1,3] and Pablo Cruz [2]

[1] Civil and Environmental Engineering Department (DECA), ETSECCPB, Universidad Politécnica de Cataluña (UPC), Campus Norte, 08034 Barcelona, Spain
[2] Applus IDIADA, Main Technical Center, Santa Oliva, 43710 Tarragona, Spain
[3] Centre Internacional de Mètodes Numèrics en Enginyeria (CIMNE), Campus Norte UPC, 08034 Barcelona, Spain
* Correspondence: eduardo.martin.santos@upc.edu; Tel.: +34-667-12-25-77

Abstract: Simulating composite material structures requires complex constitutive models, which normally require fine meshes to obtain an accurate prediction of their behavior. Pam-Crash software has been used for several years in the automotive industry and has been proved to be an efficient tool for simulating metallic structures, returning good correlations in a fast computational time. However, constitutive models for composite materials in Pam-Crash present some difficulties: some materials are not able to be suitably modeled and the predictive results depend on the mesh refinement. This work proposes a solution for predicting the progressive damage of composite materials in Pam-Crash, which scales the energy dissipated by the damage mechanisms and checks the viability of modeling the material behavior, taking into account the recommended size of finite elements in the automotive industry. The proposed solution is applied for the simulation of Open Hole specimens to evaluate the ultimate strength consistency. After this, it is applied for the simulation of Compact Tension specimens to check the consistency of crack propagation behavior. By considering the target size of the finite elements in the material card definition, the predictions demonstrate great improvement in the equivalence in results between different mesh refinements. Finally, the solution is applied to simulate impact tests on large structures. Good correlations with experimental data are obtained in fast computational times, making this methodology a candidate for application in composite-related automotive simulations.

Keywords: composite materials; low-velocity impact; virtual testing; Pam-Crash

MSC: 37M05; 70E55

check for updates

Citation: Martin-Santos, E.; Barbu, L.G.; Cruz, P. Damage and Failure Modeling of Composite Material Structures Using the Pam-Crash Code. *Mathematics* **2024**, *12*, 3847. https://doi.org/10.3390/math12233847

Academic Editor: Manuel Pastor

Received: 17 October 2024
Revised: 13 November 2024
Accepted: 21 November 2024
Published: 6 December 2024

Copyright: © 2024 by the authors. Licensee MDPI, Basel, Switzerland. This article is an open access article distributed under the terms and conditions of the Creative Commons Attribution (CC BY) license (https://creativecommons.org/licenses/by/4.0/).

1. Introduction

New concepts in the automotive industry aim to design more efficient vehicles by reducing structural weight [1–4]. This can be achieved by replacing metallic parts with new ones manufactured from composite materials, which in turn improve specific mechanical features [1,4].

In combination with this, developments in automotive frameworks involve numerous procedures where CAE tools are applied. Consequently, the introduction of new material types presents some challenges for successful component design. To ensure computational tools remain up to date and reliable, the behavior of new parts made from composite materials must be suitably simulated. Once this is achieved, the desired component and vehicle performance can be ensured while the expensive experimental test campaign required in their development can be reduced. An additional challenge is that for successful integration in the industrial process, the simulation of novel materials must be compatible with the existing procedures in automotive development. Safety regulations should include

full-vehicle impact-related scenarios. In addition to the full-vehicle structure and safety-related components, extra features are involved (i.e., bolt pre-stress, airbags, and dummies), which largely increase the complexity of the problem and, thus, the time needed to obtain the solution for the numerical analysis.

The commercially available finite element (FE) code Pam-Crash has been used in the automotive industry for several years, mainly dealing with crashworthiness simulations by using an explicit solver. It has been proven to accurately predict the behavior of large metallic structures in short simulations [5–9].

Considering that conventional metallic structures usually fail due to plastic flow [10], a significant challenge in the simulation of composite materials is caused by their failure due to a combination of interacting damage mechanisms [11,12]. For an accurate simulation, complex constitutive models, which often need the use of a refined mesh, are required. However, employing small elements in an explicit FE code implies long analysis times due to the large number of elements that must be calculated and the fact that a stable time increment for a simulation is proportional to the element size.

These last factors constitute boundaries for the composite development in the automotive industry. The application of selected materials in coarse meshes needs to be ensured, achieving proper behavior consistency in fast computation times to be used in full-vehicle simulations. Due to the complexity of these simulations regarding the consideration of a large number of materials, components and interactions, the application of customized procedures becomes forbidden (i.e., user-defined materials). To obtain suitable solutions that are widely applicable in this framework, the capabilities of the constitutive models available in commercial codes need to be explored.

The constitutive model for unidirectional plies in Pam-Crash, which is formulated in the Continuum Damage Mechanics framework, is based on the work of Ladevèze and Le Dantec [13]. In Pam-Crash implementation, it behaves in a fast and stable way for impact-related applications, making it of interest for industrial development. Despite this, some limitations are detected: damage description is performed by the input of strain-related parameters, which are influenced not only by the material properties but also by mesh refinement. In combination with the constitutive formulation implemented, this leads to some difficulties. The formulation does not account for the size of the elements in the simulation when defining their constitutive behavior, which results in the structural response being largely dependent on the mesh refinement. As a result, for a single material definition, finer meshes tend to absorb less energy during a localized fracture process than coarse meshes do. Finally, large fracture toughness leads to an undesirable increase in the ultimate strength obtained by the related constitutive law.

The present work deals with an engineering solution to suitably simulate the damage and failure of multidirectional ply-based composite materials in Pam-Crash. Development was performed with PamCrash v2018. As no significant changes have been implemented in Ply Type 1 since that version [14], the solution presented here remains valid and usable. The solution is used for the generation of a composite-related material card as part of the model's preprocessing step. It uses as inputs the material properties obtained by the characterization standards and the target element size in the simulation. Taking into account energy consistency and the different possibilities in the law definition from the constitutive model, it ensures that the defined material will behave as closely as possible to the input mechanical properties for the selected mesh refinement. For this, the solution applies the Bažant crack band method [15], where the volumetric energy dissipated by the finite elements is computed by considering their size. Since limitations for the ratio between fracture toughness and ultimate strength are detected in the constitutive formulation, the solution allows the assessment—at the material card creation stage—of when the modeling of a material in the selected FE size becomes unfeasible. This enables decision making for implementing countermeasures regarding the material card prior to the model's preprocessing stage. Although the solution does not eliminate the mesh influence, it ensures consistency in the mechanical response for elements not largely differing from the target

element size used for the computation of strain-related parameters. Ranges of about 25% under and over the target element size lead to proper correlation levels. When larger differences in element size cannot be avoided, more than one material definition will be required to ensure consistency in the behavior.

The validity of the solution is checked through the simulation of Open Hole and Compact Tension tests under tensile loading. Applying the proposed solution yields the desired response for the target mesh refinement.

Since developmental processes in the industry require testing large-scale structures [16–18], an additional objective of this work is to minimize the computational time required for their analysis. In this context, the solution is also employed to simulate a transverse low-velocity impact test on large cylindrical structures. The simulations have a low computational cost while ensuring robust experimental correlations.

This work comprehensively analyzes the constitutive model for composite materials in the PamCrash finite element method (FEM) code. Subsequently, it employs the crack band model to provide a preprocessing tool that translates material properties into the required FEM properties,ensuring robustness in the constitutive behavior of the material despite mesh refinement. The proposed methodologies can be directly integrated into current industrial developments without requiring updates to other tools and ensuring compatibility with existing model features. Consequently, composite material structures can be directly incorporated into automotive simulations to perform full-vehicle developments, such as occupant or pedestrian protection (including features like alternative materials, airbags with particle physics, human body models, etc.). The applicability of the solution is verified through simulations of impact on large composite components (800 mm in length), which are simulated under conditions analogous to those in a full-vehicle model.

2. Modeling of Unidirectional Composite Ply in Pam-Crash

The Pam-Crash material library offers two options to describe the behavior of unidirectional-reinforced composite materials: the "ply model type 0" (PMT-0), designated as a "Unidirectional Composite Bi-Phase Ply Model", defines the fibers and the matrix with independent rheological laws [19], whilst the "ply model type 1" (PMT-1), corresponding to the "Unidirectional Composite Global Ply Model", treats the composite ply as an orthotropic homogeneous material and is based on the formulation published by Ladevèze and Le Dantec [13]. This formulation considered brittle failure in the fiber direction, matrix plasticity, progressive degradation of the matrix by micro-cracking and brittle failure due to fiber–matrix debonding. The degradation of the matrix under compressive stresses was not considered. The formulation implemented for the PMT-1 includes several improvements: the transverse shear behavior based on Hurez [20] (elasticity in plane 23 and degradation in plane 13), and progressive degradation in the fiber direction, under both tensile and compressive stresses.

The PMT-1 formulation allows for the consideration of different elastic moduli for tensile and compressive stresses. Furthermore, under compressive stresses, a non-linear elasticity is considered for materials with fiber misalignments or micro-buckling phenomena [13]. Specifically, the elastic modulus in the fiber direction is defined as [19]

$$\begin{aligned} E_1 &= E_{1T} && \text{if } \sigma_1 \geq 0 \\ E_1 &= \frac{E_{1C}}{1 + \gamma E_{1C} |\varepsilon_1|} && \text{if } \sigma_1 < 0 \end{aligned} \tag{1}$$

where E_1 is the elastic modulus in the fiber direction. The subscripts T and C denote tension and compression, respectively. The parameter γ is used to account for the elastic non-linearity under compression. In the present work, a value of $\gamma = 0$ is assumed, as unidirectional carbon-based composite materials commonly exhibit linear behavior in the elastic regime. Accordingly, the Complementary Free Energy for PMT-1, E_D, can be defined as

$$E_D = \frac{\sigma_1^2}{2(1-d_1)E_1} + \frac{\sigma_2^2}{2(1-d_2)E_2} + \frac{\sigma_6^2+\sigma_4^2}{2G_{12}(1-d_6)} + \frac{\sigma_5^2}{2G_{23}} + \frac{\nu_{12}}{E_1}\sigma_1\sigma_2 + \sigma : \varepsilon^p \quad (2)$$

where σ and ε^p are the stress and the plastic-strain tensors, respectively; E_2 is the elastic modulus in the matrix direction; G_{12} and G_{23} are the in-plane and out-of-plane shear moduli, respectively; ν_{12} is the major in-plane Poisson's ratio; and d_1, d_2 and d_6 are the fiber, matrix and in-plane shear damage variables, respectively. The fiber damage variable d_1 takes the maximum value of its related tensile and compressive damage variables (i.e., d_{1T} and d_{1C}, respectively). The values of the matrix-related damage variables, d_2 and d_6, are computed using a combination of the in-plane shear and the transverse tensile effective stresses. The transverse compressive stresses do not contribute to the computation of d_2 and d_6.

From the derivative of Equation (2) with respect to the stress tensor, the constitutive law expressed in Voigt notation is

$$\begin{Bmatrix} \varepsilon_1 \\ \varepsilon_2 \\ \varepsilon_4 \\ \varepsilon_5 \\ \varepsilon_6 \end{Bmatrix} = \begin{Bmatrix} \frac{1}{(1-d_1)E_1} & -\frac{\nu_{12}}{E_1} & 0 & 0 & 0 \\ -\frac{\nu_{12}}{E_1} & \frac{1}{(1-d_2)E_2} & 0 & 0 & 0 \\ 0 & 0 & \frac{1}{(1-d_6)G_{12}} & 0 & 0 \\ 0 & 0 & 0 & \frac{1}{G_{23}} & 0 \\ 0 & 0 & 0 & 0 & \frac{1}{(1-d_6)G_{12}} \end{Bmatrix} \begin{Bmatrix} \sigma_1 \\ \sigma_2 \\ \sigma_4 \\ \sigma_5 \\ \sigma_6 \end{Bmatrix} \quad (3)$$

where ε is the elastic strain vector. It can be observed that the degradation of G_{23} is not considered in the model.

To ensure that the second principle of thermodynamics is satisfied, a positive rate of energy dissipation must be defined. From Equation (2), the dissipation is defined as

$$\Xi = Z_{d_1}\dot{d_1} + Z_{d_2}\dot{d_2} + Z_{d_6}\dot{d_6} + \sigma : \dot{\varepsilon}^p \geq 0 \quad (4)$$

In the definition of the matrix hardening, the positive rate of Ξ is ensured by enforcing the increments of the plastic strain to be proportional to the stress tensor. For the damage-related mechanisms, the damage rate must be defined as positive to ensure the irreversibility of the process. The thermodynamic forces Z_{d_N} (N =1, 2 or 6), which are obtained by the derivation of Equation (2) with respect to the damage variables, are defined as

$$\begin{aligned} \frac{\partial E_D}{\partial d_1} &= Z_{d_1} = \frac{1}{2}\frac{\sigma_1^2}{E_1(1-d_1)^2} \geq 0 \\ \frac{\partial E_D}{\partial d_2} &= Z_{d_2} = \frac{1}{2}\frac{\langle\sigma_2\rangle^2}{E_2(1-d_2)^2} \geq 0 \\ \frac{\partial E_D}{\partial d_6} &= Z_{d_6} = \frac{1}{2}\frac{\sigma_6^2+\sigma_4^2}{G_{12}(1-d_6)^2} \geq 0 \end{aligned} \quad (5)$$

where $\langle x\rangle$ are the Macaulay brackets, which are defined as $\langle x\rangle = (x + |x|)/2$.

2.1. Fiber Behavior

The damage evolution functions over the time t for the fiber-related mechanisms, $\mathcal{Y}_{1I}^{(t)}$, are defined from the thermodynamic force Z_{d_1}. According to the Pamcrash solver reference manual, the coupling between tension and compression mechanisms is not considered. Each damage evolution function takes the maximum value achieved during the analysis [19]:

$$\mathcal{Y}_{1I}^{(t)} = \max\left\{\mathcal{Y}_{1I}^{(t-1)}, \sqrt{Z_{d_1}^{(t)}}\right\} \ \forall t \geq 0 \quad \text{with } I = \begin{cases} C \text{ if } \sigma_1 \leq 0 \\ T \text{ if } \sigma_1 > 0 \end{cases} \tag{6}$$

In the PMT-1 constitutive model, fiber-related damage variables are defined as a linear function of ε_1 [13]. Thus, from the definition of $\mathcal{Y}_{1I}$, it can be expressed as (hereafter, the time t is implicitly included)

$$d_{1I} = \min\left\{d_{1I}^u \frac{\langle \mathcal{Y}_{1I} - \mathcal{Y}_{1I}^i \rangle}{\mathcal{Y}_{1I}^u - \mathcal{Y}_{1I}^i}, 1 - (1 - d_{1I}^u)\frac{\mathcal{Y}_{1I}^u}{\mathcal{Y}_{1I}}\right\} \tag{7}$$

where $\mathcal{Y}_{1I}^i$ and $\mathcal{Y}_{1I}^u$ are the values of $\mathcal{Y}_{1I}$ for damage onset and damage propagation, respectively. When $\mathcal{Y}_{1I}^u$ is reached, d_{1I} grows asymptotically toward unity, ensuring a constant residual stress $\sigma_r = (1 - d_{1I}^u)E_1\varepsilon_{1I}^u$, where ε_{1I}^u is the strain for damage propagation and d_{1I}^u is an input parameter defined below and close to unity. Finally, a single fiber damage variable is used for tension and compression loading; thus, $d_1 = \max\{d_{1T}, d_{1C}\}$.

Under uniaxial loading, the damage evolution function can be expressed as a function of the strain ε_1:

$$\mathcal{Y}_{1I}^{(t)} = \max\left\{\mathcal{Y}_{1I}^{(t-1)}, \left|\varepsilon_1^{(t)}\right|\sqrt{\frac{E_1}{2}}\right\} \ \forall t \geq 0 \tag{8}$$

According to Equation (8), d_{1I} can alternatively be expressed as a linear function of the strain:

$$d_{1I} = \min\left\{d_{1I}^u \frac{\langle |\varepsilon_1| - \varepsilon_{1I}^i \rangle}{\varepsilon_{1I}^u - \varepsilon_{1I}^i}, 1 - (1 - d_{1I}^u)\frac{\varepsilon_{1I}^u}{|\varepsilon_1|}\right\} \tag{9}$$

where ε_{1I}^i and ε_{1I}^u are the values of ε_1 for damage onset and damage propagation, respectively. According to Equations (7) and (9), three loading phases can be identified: elastic $|\varepsilon_1| < \varepsilon_{1I}^i$, linear damage $\varepsilon_{1I}^i \leq |\varepsilon_1| < \varepsilon_{1I}^u$, and asymptotic damage $\varepsilon_{1I}^u \leq |\varepsilon_1|$ (i.e., residual stress phase).

The degradation process of the constitutive law follows a parabola-shaped profile which can be characterized by three key points: the damage onset $(\varepsilon_{1I}^i, X_{1I}^i)$, where $X_{1I}^i = E_1\varepsilon_{1I}^i$; the critical stress point $(\varepsilon_{1I}^c, X_{1I}^c)$; and the residual stress point $(\varepsilon_{1I}^u, \sigma_r)$. Given that X_{1I} is the material strength in the fiber direction, two different constitutive laws can be obtained. If $\varepsilon_{1I}^i < \varepsilon_{1I}^c$, the maximum stress is X_{1I}^c (i.e. $X_{1I}^i < X_{1I}^c$ and $X_{1I}^c = X_{1I}$), which leads to ductile failure. Then, two sequential degradation phases are taken into account (hereafter referred to as behavior F2; see Figure 1a). However, if $\varepsilon_{1I}^i \geq \varepsilon_{1I}^c$, the maximum stress is X_{1I}^i (i.e. $X_{1I}^i = X_{1I}$), which leads to a quasi-brittle failure. Then, a single degradation phase is taken into account (hereafter referred to as behavior F1; see Figure 1b).

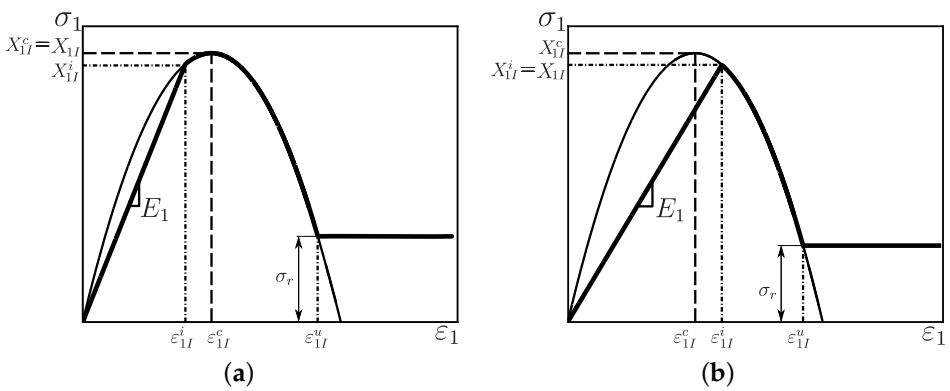


Figure 1. Constitutive law for uniaxial loading in the fiber direction: (**a**) with two sequential degradation phases (referred to as F2), and (**b**) with a single degradation phase (referred to as F1).

By equating the derivative of the constitutive law to zero, the critical point is defined as

$$\varepsilon_{1I}^{c} = \frac{\varepsilon_{1I}^{u} - (1 - d_1^u)\varepsilon_{1I}^{i}}{2d_1^u} \quad , \quad X_{1I}^{c} = \frac{E_1\left(\varepsilon_{1I}^{u} - (1 - d_1^u)\varepsilon_{1I}^{i}\right)^2}{4d_1^u\left(\varepsilon_{1I}^{u} - \varepsilon_{1I}^{i}\right)} \tag{10}$$

It is worth noting that if σ_r is zero (i.e., $d_{1I}^{u} = 1$), the critical point of Equation (10) is simplified to

$$\varepsilon_{1I}^{c} = \frac{\varepsilon_{1I}^{u}}{2} \quad , \quad X_{1I}^{c} = \frac{E_1\left(\varepsilon_{1I}^{u}\right)^2}{4\left(\varepsilon_{1I}^{u} - \varepsilon_{1I}^{i}\right)} \tag{11}$$

The inputs required to define the constitutive behavior of PMT-1 in the fiber direction are the parameters of Equation (9): ε_{1I}^{i}, ε_{1I}^{u} and d_{1I}^{u}. The strain-based inputs should be defined by the longitudinal material properties obtained from experimental coupon tests: elastic modulus, E_1; strength, X_{1I}; and fracture toughness, $\mathcal{G}_{X_{1I}}$. The proposed solution, which defines the strain-based inputs by taking into account the material properties and the finite element size, is presented in Section 3.2. The solution ensures the objectivity of the numerical solution under mesh refinement.

2.2. Matrix Behavior

2.2.1. Damage

From the thermodynamic forces of Equation (5), two damage evolution functions over time t are defined [13]:

$$\mathcal{Y}_{eq}^{(t)} = \max\left\{\mathcal{Y}_{eq}^{(t-1)}, \sqrt{Z_{d_6}^{(t)} + bZ_{d_2}^{(t)}}\right\} \quad \forall t \geq 0 \tag{12}$$

$$\mathcal{Y}_{br}^{(t)} = \max\left\{\mathcal{Y}_{br}^{(t-1)}, \sqrt{Z_{d_2}^{(t)}}\right\} \quad \forall t \geq 0 \tag{13}$$

The function $\mathcal{Y}_{eq}$ is used to describe the progressive damage for the transverse tensile and shear constitutive laws under combined loading conditions, where the parameter b accounts for the ratio of the transverse tensile stress that contributes to $\mathcal{Y}_{eq}$. The function $\mathcal{Y}_{br}$ defines brittle failure occurrence as a function of the transverse tensile stress.

Three different options are available in PMT-1 to define the damage variables as a function of $\mathcal{Y}_{eq}$ and $\mathcal{Y}_{br}$: linear, exponential and tabular [19]. The linear and exponential options are described herein.

The linear damage function is defined as

$$d_M = \begin{cases} \dfrac{\langle \mathcal{Y}_{eq} - \mathcal{Y}_M^i \rangle}{\mathcal{Y}_M^u - \mathcal{Y}_M^i} & \text{if } \mathcal{Y}_{br} < \mathcal{Y}_{br}^c, \mathcal{Y}_{eq} < \mathcal{Y}_M^u \text{ and } \mathcal{Y}_{eq} < \mathcal{Y}_{eq}^c \\ 1 & \text{otherwise} \end{cases} \tag{14}$$

where M can take the values 2 and 6, which refer to the transverse and shear directions, respectively. Four input parameters are required to define the matrix degradation in PMT-1: $\mathcal{Y}_M^i$ and $\mathcal{Y}_M^u$, which refer to the damage onset and damage propagation thresholds, respectively. The parameters $\mathcal{Y}_{br}^c$ and $\mathcal{Y}_{eq}^c$ are two optional inputs which refer to the limits for brittle failure under transverse tensile loading and under combined transverse tensile and in-plane shear loading, respectively. The damage variable d_M can be defined as a function of the strains, as is shown for fiber damage in Equation (9), using the thermodynamic forces of Equation (5), and the damage evolution functions defined by Equations (12) and (13). Consequently, the constitutive laws obtained are similar to those shown in Figure 1 without considering residual stress.

The exponential function of the damage variables, on the other hand, is based on the formulation proposed by Greve and Pickett [21], which defines

$$d_M = \begin{cases} d_{sat_M}\left(1 - e^{\frac{-\langle \mathcal{Y}_{eq} - \mathcal{Y}_M^i \rangle}{\mathcal{Y}_M^u - \mathcal{Y}_M^i}}\right) & \text{if } \mathcal{Y}_{br} < \mathcal{Y}_{br}^c \text{ and } \mathcal{Y}_{eq} < \mathcal{Y}_{eq}^c \\ d_{sat_M} & \text{otherwise} \end{cases} \tag{15}$$

where d_{sat_M} is the saturation damage factor.

2.2.2. Plasticity

To describe the mechanisms that cause permanent transverse and shear strains, an isotropic-hardening plasticity model is defined in PMT-1, which is based on the formulation of Ladevèze and Le Dantec [13]. The yield function is expressed as

$$\mathcal{F}_P = \sqrt{\left(\frac{\sigma_6}{1-d_6}\right)^2 + A\left(\frac{\langle \sigma_2 \rangle}{1-d_2} + \langle -\sigma_2 \rangle\right)^2} - R_0 - B(\varepsilon_{eq}^p)^m \leq 0 \tag{16}$$

where ε_{eq}^p is the equivalent plastic strain, R_0 is the yield stress, B is the hardening law multiplier and m is the hardening law exponent. The parameter A couples the shear and transverse plastic strains. The parameters R_0, B, m and A are the input parameters for PMT-1. The procedures to fit these parameters from experimental tests are presented in Ladevèze and Le Dantec [13] or in O'Higgins and McCarthy [22]. The matrix in the composite follows an associative plasticity in which the potential for the plastic flow is defined as

$$\dot{\varepsilon}^p \propto \frac{\partial \mathcal{F}_P}{\partial \sigma} \tag{17}$$

These definitions for $\mathcal{F}_P$ and $\dot{\varepsilon}^p$ ensure that the positive rate of dissipation in Equation (4) is trivially satisfied.

2.2.3. Yield and Failure Functions

Once the evolution of the damage variables and the criteria for plasticity are defined, the envelopes for the onset of non-linearities in matrix-related mechanisms can be sketched, as shown in Figure 2. $\widetilde{\sigma}_2$ and $\widetilde{\sigma}_6$ are the effective stresses computed using Equation (3) for an undamaged state. In this diagram, the region between the origin and any line represents the elastic regime in the material's behavior. Once the dark dotted line is surpassed, plasticity onset occurs and evolves with stress increase. The solid line indicates the onset of material degradation, which progresses to total failure at the light-dotted line. Two notable effects on this envelope can be observed: for nearly pure tensile states, damage occurs before plasticity. This occurs because the fibers in the transverse direction limit the matrix plastic flow. The other effect that can be seen is that the evolution of compressive forces triggers plasticity but not damage for matrix-related mechanisms.

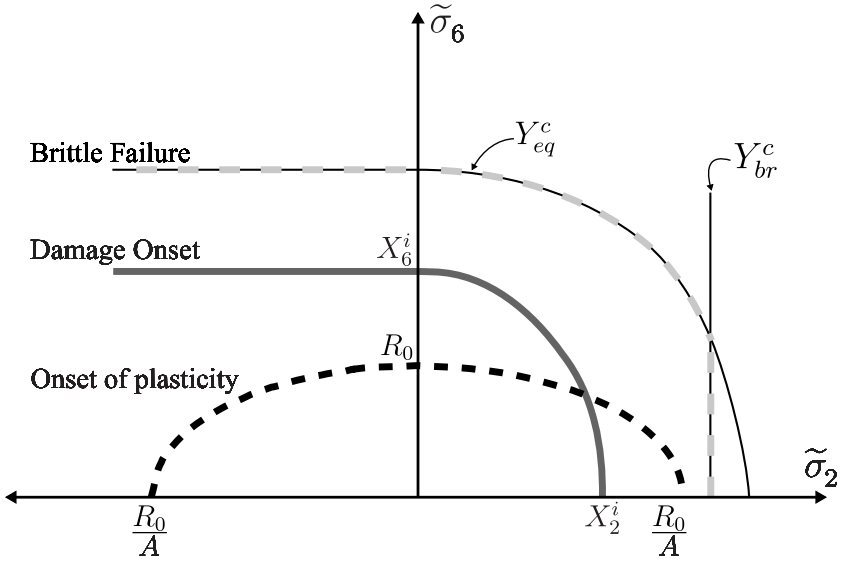


Figure 2. Envelopes for the onset of non-linearities in matrix-related mechanisms (with scaled parameters for an easier interpretation of their meaning).

3. Model Calibration

The Pam-Crash "Solver Notes Manual" [19] calibrates the model with the following tests:

- Fiber-related mechanisms: simple tension and compression tests on $[0]_8$ laminates.
- Matrix-related mechanisms, associated with damage and plasticity: cyclic tensile tests on $[\pm 45]_{2s}$ for the extraction of the shear-related properties, and $[\pm 67.5]_{2s}$ for the transverse properties.

The calibration of the model presented by Ladevèze and Le Dantec [13] does not require testing the $[45]_8$ laminate. This is beneficial because the lack of material symmetry in experimental tests on $[45]_8$ laminates causes a misalignment in the load path and thus creates moments, which can lead to improper data reading, making data reduction difficult. Despite this, the Pam-Crash "Solver notes manual" [19] recommends it for the determination of the coupling parameter between transverse and shear strains and for ensuring the measurement of the transverse modulus.

A comparison of different methods for adjusting the parameters related to the transverse behavior is presented by O'Higgins and McCarthy [22]. The fitting methodologies for non-linear response presented by Ladevèze and Le Dantec [13] or those presented by O'Higgins and McCarthy [22], and those summarized in the Pam-Crash Solver notes manual [19] offer reliable methods for adjusting the hardening response of the material, which are mainly related to shear plasticity. Therefore, after a brief introduction to plasticity in shear response, this section is mainly focused on defining mesh-independent material properties for damage propagation.

3.1. Shear Response

The $[\pm 45]_{2s}$ specimen results in an almost pure shear stress in the ply; therefore, the stress (σ) and strain (ε) applied to the specimen can be transformed to a shear stress and strain in the ply as $\sigma_6 = \sigma/2$ and $\varepsilon_6 = \varepsilon - \varepsilon_T$, where ε_T is the transverse strain of the specimen. This test allows the shear modulus (G_{12}) to be defined and the measurement of plastic strains with the evolution of the load to be taken. By carrying out several load–unloading cycles whilst the test is performed, it is possible to measure the decrease in shear modulus caused by damage effects.

For this purpose, the Pam-Crash manual recommends having at least 5 loading/unloading quasi-static cycles until specimen failure to ensure a minimum quantity of data to compute reliable damage evolution.

The parameters $\mathcal{Y}_6^i$ and $\mathcal{Y}_6^u$ from Equations (14) or (15), depending on whether the linear or exponential damage law is selected, can be determined by fitting the experimental results d_6 with respect to $\mathcal{Y}_{eq}^{(t)} = \sqrt{2G_{12}}(\varepsilon_6 - \varepsilon_6^p)$. The plastic parameters R_0, B and m are obtained from the same test by fitting the functions

$$\sigma_6 = R_0 + B(\varepsilon_{eq}^p)^m \quad \text{where} \quad \varepsilon_{eq}^p = \int (1 - d_6)\dot{\varepsilon}_6^p dt \tag{18}$$

to the experimental stress (σ_6), damage (d_6) and plastic strain (ε_6^p) [19].

The coupling parameter A in Equation (16) can be determined by loading and unloading the $[\pm 67.5]_{2s}$ specimen. As in the damage evolution determination procedure, a minimum of five quasi-static loading/unloading cycles is recommended to acquire sufficient data for the computation of reliable values for this parameter.

The parameter A is defined as

$$A = \frac{\dot{\varepsilon}_2^p (1 - d_2)^2}{\dot{\varepsilon}_6^p (1 - d_6)^2} \tag{19}$$

In this study, the composite materials analyzed are composed of carbon fibers and epoxy matrix. Due to their configuration and quality, the plastic component in the transverse direction becomes negligible, so a coupling factor of zero is assumed.

3.2. Energy Regularization

The stress–strain constitutive response of quasi-brittle materials shows a softening behavior once the ultimate strength is reached, leading to strain localization. At that point, the constitutive law can no longer be expressed as a stress–strain relationship and must be rewritten in the form of a cohesive law, which is expressed in terms of stress and crack opening displacement [23]. When a softening degradation process is implemented in a volumetric FE model, the dissipated energy depends on the size of the elements [24–26]. Therefore, the use of different mesh refinements to simulate the same structure can result in differing amounts of dissipated energy and, thus, different global structure response predictions.

Employing the crack band model proposed by Bažant and Oh [27] ensures the objectivity of the finite element model by regularizing the computed dissipated energy for each failure mechanism, using a characteristic length of the finite element and the corresponding fracture toughness.

Since the formulation of the PMT-1 does not include any regularization of the energy dissipated due to the damage process, the effect mentioned above can occur: the use of different mesh refinements to solve equivalent simulations can result in differing amounts of dissipated energy once damage is initiated, predicting different global structure responses.

3.2.1. Numerical Methodology

Cohesive laws are usually defined for elements with zero thickness, since they are formulated to define crack propagation but not the field of strains around it. If a cohesive law is applied to volumetric elements, the energy dissipated by the damage process becomes dependent on their thickness. To avoid this, different solutions have been proposed in the literature. The smearing of the crack in the thickness of the whole element is one of the most commonly applied solutions. Known as the "crack band model", it has been proved to be an efficient method for obtaining energy dissipation independent of mesh refinement [12,28,29]. Another method to minimize the influence the mesh may have on the numerical response is the non-local approach. This was used in combination with the Ladevèze and Le Dantec constitutive model by Frizzell et al. [30,31].

Following the strain localization, this method defines the behavior of the point by taking into account the state of the material in a defined volume surrounding it. In this case, besides reducing the influence the mesh refinement has on the energy dissipated,

another advantage is gained: the crack propagation loses its tendency to align with the lines in the mesh. Nevertheless, this method increases the computational cost of performing the analysis. In Ladevèze et al. [32], the constitutive model was improved by using a delay on the damage evolution. This delay acts as a viscous-type regularization, which is another method used to reduce the influence that the mesh refinement has on the numerical solution.

3.2.2. Proposed Solution for PMT-1

To implement the solution presented here, the crack band model algorithm was the method adopted to reduce the influence of the mesh refinement on the numerical simulations. Since this method controls the amount of energy dissipated by the finite elements, the solution is formulated considering the elements able to be fully damaged during the analysis (i.e., $d^u_{NI} = 1$ in Equation (7) or $d_{sat_M} = 1$ in Equation (15)).

The formulation of the PMT-1 considers a linear evolution of the damage variables with their strains for the fiber-related mechanisms. For the matrix-related mechanisms, the option to define an exponential evolution of the damage variable is available. In both of the formulations included in the PMT-1, two different types of behavior can be defined. These depend on the ratio between the initial and ultimate strains used to define the material cards: a softening behavior is defined when ε^i_{NI} matches with the maximum load in the constitutive law. Under this condition, the stiffness is linear until the ultimate strength, X_{NT}, is achieved and then drops from this point until the ultimate strain, ε^u_{1I}, is reached (Figure 3a). If the value of $\varepsilon^u_{NI}/\varepsilon^i_{NI}$ is greater than 2, before the softening, a hardening behavior is observed in the constitutive law, and the ultimate strength of the material does not match the strain at which damage onset occurs (Figure 3b).

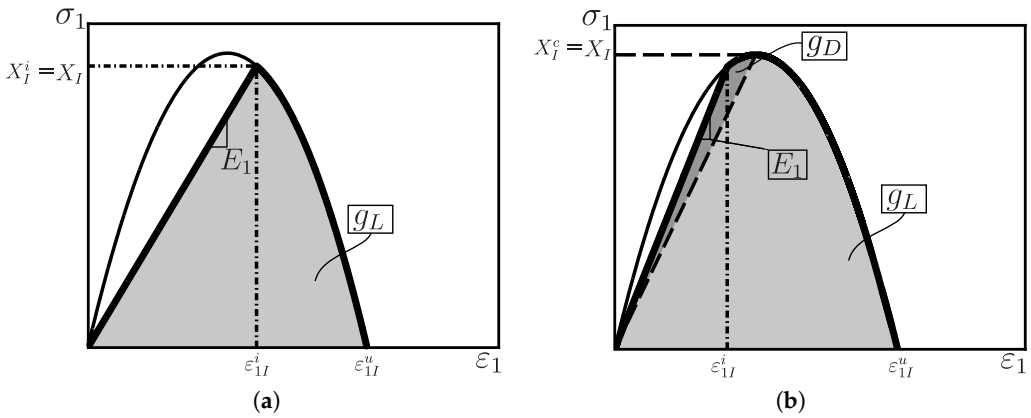


Figure 3. Schema of the two types of behavior available in the PMT-1: (**a**) softening and (**b**) hardening-softening behavior.

From the constitutive relationship in Equation (3), and the damage definitions for the fiber-related mechanisms (Equation (9)) or the damage definitions for the matrix-related mechanisms in Equation (14), the constitutive law for the mechanisms in which the damage variable follows a linear evolution can be obtained. The ultimate strength is defined as

$$X_{NI_{lin}} = \begin{cases} E_N \varepsilon^i_{NI} & \text{if } \varepsilon^u_{NI} < 2\varepsilon^i_{NI} \\ \frac{E_N \left(\varepsilon^u_{NI}\right)^2}{4\left(\varepsilon^u_{NI} - \varepsilon^i_{NI}\right)} & \text{if } \varepsilon^u_{NI} > 2\varepsilon^i_{NI} \end{cases} \tag{20}$$

For the exponential evolution of damage in the matrix-related mechanisms, the constitutive relationship in Equation (3) and the damage definition from Equation (15) can be used to obtain the constitutive law. The ultimate strength in this case is defined as

$$X_{M_{exp}} = \begin{cases} E_M \varepsilon_M^i & \text{if } \varepsilon_M^u < 2\varepsilon_M^i \\ E_M e^{\frac{2\varepsilon_M^i - \varepsilon_M^u}{\varepsilon_M^u - \varepsilon_M^i}} (\varepsilon_M^u - \varepsilon_M^i) & \text{if } \varepsilon_M^u > 2\varepsilon_M^i \end{cases} \quad (21)$$

Figure 4 shows the distribution of stresses in a cracked specimen. When a defect such as a crack or a notch is present in a loaded material, three different stress regions can be identified [33]. Region *a* is the linear elastic zone, where the material is working in an elastic regime, while region *b* is the hardening zone; the material in this zone is damaged by intrinsic degradation: inelastic mechanisms are affecting the mechanical properties of the material, but the ultimate strength is still not reached (i.e., hardening due to matrix plasticity). The energy dissipated by the intrinsic degradation in the constitutive law is defined as g_D in Figure 3. The zone in which these mechanisms are present is located in the volume surrounding the crack. Finally, region *c* is the softening zone, which corresponds to the region of localized strains. The material in this zone is being degraded by extrinsic mechanisms that cause crack propagation and thus a dissipation of energy, which is defined as g_L in Figure 3.

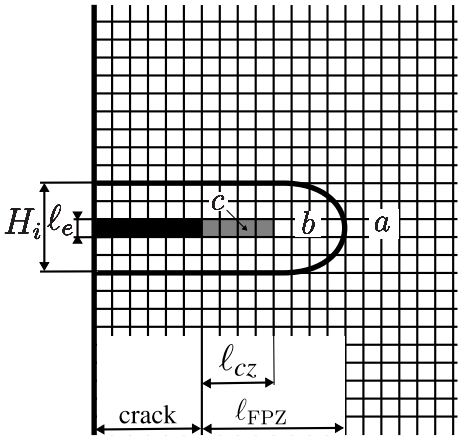


Figure 4. Crack growth in the discretized continuum with the elastic (*a*), non-linear hardening (*b*) and softening (*c*) regions.

The fracture toughness of the material is determined by considering the contributions from both extrinsic and intrinsic mechanisms. Dissipation, with respect to crack increase due to the extrinsic mechanisms, is localized in the failure plane and is determined by $g_L \ell_e$ in the numerical simulations. On the other hand, intrinsic dissipation occupies a certain volume surrounding the crack. In this case, dissipation resulting from the intrinsic mechanisms is usually larger than $g_D \ell_e$ due to the non-localized damage contribution. In quasi-brittle materials, the volume occupied by the non-localized damage tends to zero, and therefore its contribution in the numerical simulations can be considered as $g_D \ell_e$.

In this case, when combined with the crack band model, a limitation on the PMT-1 formulation can be observed. The regularization of the fracture toughness by means of the element size assumes a direct influence over the ratio of strains for damage onset and ultimate degradation. Due to this, a material mechanism definition in coarser meshes will show a pure softening behavior: the ultimate strain tends to the strain for damage onset with the enlargement of the element until the snap-back effect is achieved. On the other hand, for finer meshes, the behavior of the same material would tend to a hardening–softening behavior: the ultimate strain should become larger to ensure a consistent amount of fracture toughness. Due to the formulation of PMT-1, however, if $2\varepsilon^i < \varepsilon^u$, hardening–softening behavior (F2) is triggered, where an increase in force is obtained after damage onset. From this point, an enlargement of the ultimate strain causes a proportional enlargement of the ultimate strength in the constitutive law. When $2\varepsilon^i < \varepsilon^u$, the presented solution makes the strain for damage onset tend to 0 to avoid this ultimate strength increase. As a consequence of this, for the same analysis, a component with a coarse mesh would show damage only

after the ultimate strength, while a fine mesh could show damage prior to it (i.e., in fine meshes, structures could show slightly softer behavior just before achieving the maximum force supported). In crashworthiness analysis, this effect is of minor importance, since the relevant data are the capacity for energy absorption in the material. The proposed solution ensures mesh-independent energy dissipation, but it is not possible to improve the precision for damage onset detection in fine meshes.

The energy dissipated by a crack propagation that affects the linear evolution-related mechanisms can be defined by integrating the constitutive equation under uniaxial loading.

$$\frac{\mathcal{G}_{NI}}{\ell_e} = g_L + g_D = E_N \frac{(\varepsilon^u_{NI})^3 - (\varepsilon^i_{NI})^3}{6(\varepsilon^u_{NI} - \varepsilon^i_{NI})} \tag{22}$$

And the energy dissipated by a crack propagation that affects the exponential evolution-related mechanisms can be defined as

$$\frac{\mathcal{G}_{NI}}{\ell_e} = g_L + g_D = E_M((\varepsilon^u_M)^2 - \varepsilon^i_M \varepsilon^u_M - 0.5(\varepsilon^i_M)^2) \tag{23}$$

Taking into account the definitions for the ultimate strength and the fracture toughness (Equations (20) and (22), respectively, for the linear formulation, or Equations (21) and (23) for the exponential one), the expression to ensure the correct dissipation of energy depends exclusively on a dimensionless factor, which is defined in a common form for both formulations as

$$\alpha = \frac{X^2_{NI} \ell_e}{E_{NI} \mathcal{G}_{NI}} \tag{24}$$

The parameter α is computed by means of the material properties and the size of the elements in the mesh. The magnitude of this factor shows the viability of modeling the constitutive law of the material with the selected mesh refinement. In this form, for the linear evolution of the damage variable, a value below 0.375 is too low and indicates that the fracture toughness of the material cannot be achieved without an increase in the ultimate strength. A value over 2 means that the elastic energy required to achieve the ε^i_{NI} is larger than the fracture toughness of the material: a behavior known as the snap-back effect. Within the range in which the factor α takes suitable values ($0.375 < \alpha < 2$), a value below or equal to 0.8571 ($\alpha \leq 0.8571$) indicates a hardening–softening behavior. If α takes values over 0.8571, the material is exhibiting a softening behavior.

For the exponential evolution of the damage variable, the α factor is computed in the same way, but the ranges that define the viability of modeling the material or the type of constitutive law obtained are slightly different from those in the linear evolution: in this case, a value below 0.1385 indicates that the material cannot be modeled with the selected combination of fracture toughness, element size and ultimate strength. A value between 0.1385 and 0.4 results in a hardening–softening behavior, and a value between 0.4 and 2 results in a softening behavior. Meanwhile, a value over 2 causes the snap-back effect in the same manner as in the linear evolution.

Solving Equations (20) and (22) for the linear evolution or (21) and (23) for the exponential evolution, two curves are obtained, which relate the α parameter obtained from Equation (24) with the strain for damage onset and ultimate degradation by means of the β parameters. β_i and β_u are defined by the ratio between the damage onset and ultimate strains, respectively, with the theoretical strain for damage onset X_N/E_N. This coincides with ε^i_{NI} for mechanisms showing softening behavior, where $\beta_i = 1$:

$$\varepsilon^i_{NI} = \beta_i \frac{X_{NI}}{E_{NI}} \quad \text{and} \quad \varepsilon^u_{NI} = \beta_u \frac{X_{NI}}{E_{NI}} \tag{25}$$

Figures 5 and 6 show in a graphical form the direct relation between the parameters α and β for the linear and the exponential definitions, respectively.

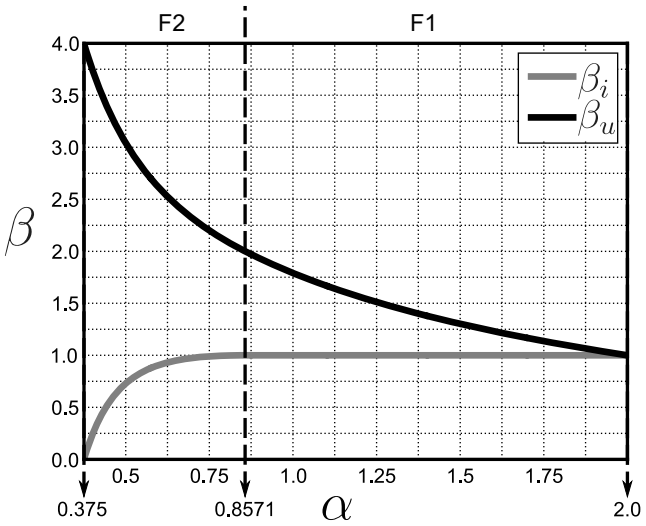


Figure 5. Evolution of the β parameters with the α factor for the linear damage law. Region F1 defines a softening behavior. Region F2 defines a hardening–softening behavior.

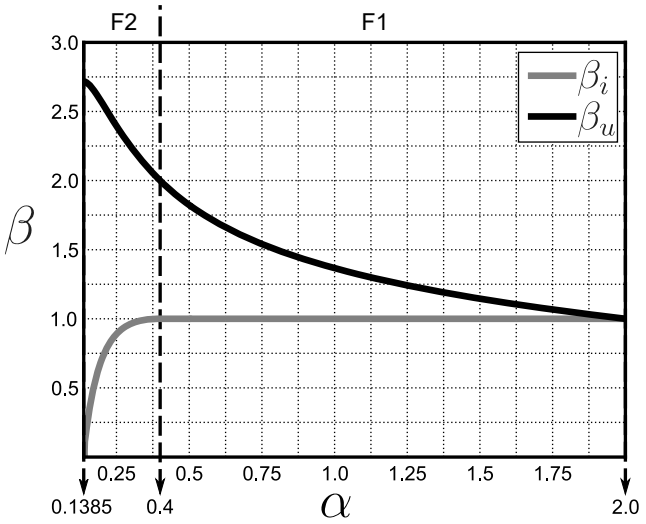


Figure 6. Evolution of the β parameters with the α factor for the exponential damage law. Region F1 defines a softening behavior. Region F2 defines a hardening–softening behavior.

The stiffness E_{NI} and strength X_{NI} in Equations (24) and (25) are material properties E_1 and X_T for tension loads in the longitudinal direction, E_1 and X_C for compressive loading in the longitudinal direction and E_2 and Y_T for transverse tension loads. All of these properties can be obtained from ASTM standards. The fracture toughness $\mathcal{G}_{NI}$ in Equation (24) should be defined for the transverse and longitudinal directions both in tension and in compression. For the transverse loading, it is quite common to use the interface fracture toughness determined with the DCB specimen. To define the longitudinal fracture toughness, the Compact Tension and Compact Compression are the specimens most commonly used [34–36].

A method for the determination of the matrix-related properties is described in the Pam-Crash manual [19]. Despite this, this method requires additional tests and does not couple the damage onset for matrix-related mechanisms: it allows the presence of a crack in shear or transverse mechanisms while the other remains pristine. Although their effects on the global behavior of the material can be different, when damage exists in a material component (i.e., matrix in a composite), to be consistent, it should be triggered for all the related mechanisms. In the following paragraphs, an alternative method is presented for

ensuring consistency in the onset of damage mechanisms, which additionally allows for a reduction in the characterization campaign proposed in the Pam-Crash manual.

To define the matrix-related mechanisms in both the linear and exponential formulations, the associated thermodynamic forces must be computed for introduction into their corresponding material cards. Fracture toughness for input into the proposed solution is extracted from delamination tests, and the remaining properties are extracted from tensile tests in the transverse and shear directions. The solution can then be applied using the matrix-related material properties. From the strain parameters obtained by applying the proposed solution and the definition of the thermodynamic forces in Equation (12), the parameters to define the matrix-related constitutive laws can be expressed as

$$\mathcal{Y}_2^i = \sqrt{\frac{bE_2}{2}}\varepsilon_2^i \quad \text{and} \quad \mathcal{Y}_2^u = \sqrt{\frac{bE_2}{2}}(\varepsilon_2^u - \varepsilon_2^i) \tag{26}$$

Since d_2 and d_6 are both related to $\mathcal{Y}_{eq}$ and both describe the same damage mechanism (i.e., matrix damage), it is proposed herein that their onset should occur simultaneously. Accordingly, parameter b is simply calculated by equalling $\mathcal{Y}_2^i$ and $\mathcal{Y}_6^i$:

$$b = \frac{2}{E_2}\left(\frac{\mathcal{Y}_6^i}{\varepsilon_2^i}\right)^2 \tag{27}$$

4. Numerical Validation

4.1. Tensile Open Hole Correlation

To demonstrate the application of the proposed solution, an Open Hole (OH) test under tensile load is simulated. Numerical models using different mesh refinements in the failure plane are solved in two sets of simulations. The first set is solved without applying the regularization for the energy dissipated by the damage mechanisms, whilst for the second set, the same selected mesh refinements are solved using the proposed method. As such, any improvement produced by applying the proposed solution can be verified; i.e., mesh dependence in the numerical simulations should be reduced, resulting in similar force–displacement responses for all models. Table 1 shows the properties used for the description of the composite material's behavior.

Table 1. Properties of the composite plies for the OH simulations.

Elastic Modulus	E_1	60	GPa
	E_2	8.8	GPa
Shear Modulus	G_{12}	4.67	GPa
Poisson Ratio	ν_{12}	0.26	-
Ultimate Strength	X_1	1000	MPa
Fracture Toughness	$\mathcal{G}_{X_1}$	42	N/mm

Numerical models in this section are merely used to check the mesh influence on structural response. Test configurations and material properties were set to study the effect of applying the solution. For this, the following considerations were taken:

- Unidirectional laminate to study single material laws without the influence or coupling of other damage mechanisms.
- Stress concentration to obtain a cohesive zone for studying mesh influence, leading to localized crack onset and propagation.
- Specimen dimensions and open hole to be able to model the defect (hole) in different mesh refinements with sufficient precision.
- Material properties set to be representative of composite materials and to have valid ranges of α in the target mesh refinements (1 to 5 mm element length).

With these boundaries, the influence of the proposed solution on the numerical response is meant to be studied. As a result of the problem boundaries, an Open Hole specimen 200 mm long, 101.6 mm wide, 4 mm thick and with a hole radius of 6.35 mm is modeled. Numerical models are performed by stacking the whole material into the thickness of one shell element. The Pam-Crash library material model 131 is used, as it is compatible with both the classical laminate theories and constitutive models for composite plies. The PMT-1 is used to define the constitutive behavior of the elementary ply. Different mesh refinements are tested, considering element sizes from 1 to 3 mm in the damage zone, with intervals of 0.5 mm, as listed in Table 2. Some examples of the meshes used in the numerical models for the simulation of the Open Hole test are shown in Figure 7.

Table 2. Element sizes with their correspondent α values and Pam-Crash input strains.

Element Size (mm)	α	ε_{1T}^{i} (%)	ε_{1T}^{u} (%)
1.0	0.398	0.368	6.288
1.5	0.597	1.510	4.371
2.0	0.796	1.665	3.517
2.5	0.996	1.670	3
3.0	1.195	1.670	2.615

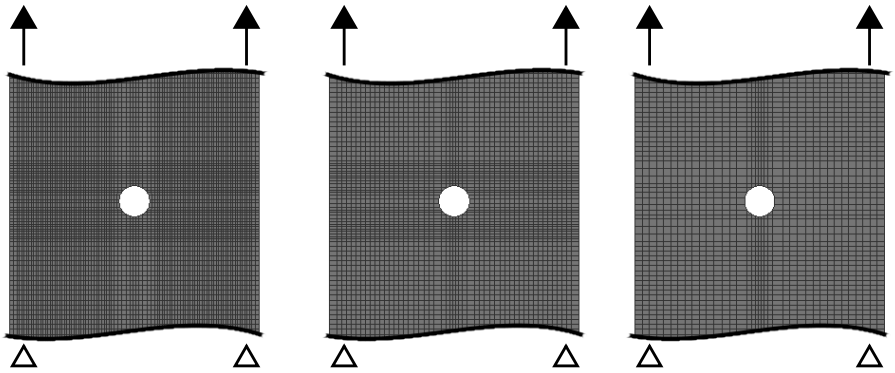


Figure 7. Example of some of the mesh refinements used in the OH simulations. left: $\ell_e = 1$ mm, centre: $\ell_e = 2$ mm, right: $\ell_e = 3$ mm.

To determine the strain properties that define the material behavior in Pam-Crash, the factor α must be computed for each of the selected mesh refinements. In this way, the first set of simulations is solved by applying the strain parameters obtained for the most refined mesh. For the second set, each model is defined by applying the strain parameters computed with regard to the size of the elements in the failure area of the modeled specimen. Table 2 summarizes the relationship between the different lengths used for the elements in the failure area. Taking into account the properties in Table 1, the range of valid sizes for the finite elements to obtain valid α values extends from 1 to 5 mm. However, meshes with element lengths above 3 mm result in a poor representation of the hole geometry in the specimen. Considering these factors, a range of elements with lengths from 1 to 3 mm has been selected. Using the size of the elements and the material properties listed in Table 1, the value for the α factor corresponding to each material definition is computed using Equation (24). Once the value for the α factor in each model is obtained, its application to the curves in Figure 5 yields the β parameters, which are then used to compute the strain parameters ε_i and ε_u by means of Equation (25). Table 2 shows the values taken by the α factors and the strain parameters obtained for the models in this set of simulations.

With the introduction of the strain parameters obtained in Table 2, all the different element sizes should yield equivalent constitutive laws for the tensile fiber mechanism, except for the fracture toughness in the material, which is scaled according to the element length to ensure proper crack energy dissipation [15].

The ultimate strengths achieved when simulating the Open Hole tensile tests are shown in Figure 8. The simulations in which the proposed solution is not implemented show a linear trend where the maximum strength supported by the specimen increases with the size of the elements in the damage zone.

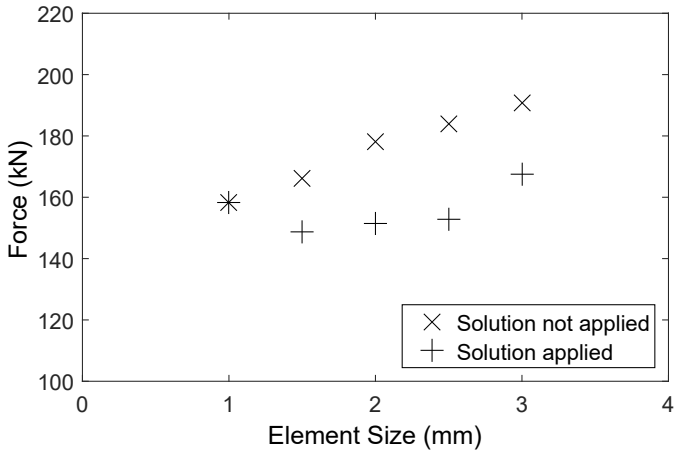


Figure 8. Strength results for the Open Hole simulations.

In the models where the solution is applied, the maximum strength supported by the specimen shows a stable zone between the sizes ℓ_e = 1.5 mm and ℓ_e = 2.5 mm, within which the maximum value of the strength supported by the specimen exhibits small variations.

Outside this range, there are some effects that limit the successful application of the solution: The model with ℓ_e= 3.0 mm has poor hole discretization. In this case, loading conditions in the damage onset zone change sufficiently to reduce the stress triaxiality. This causes an increase in the force that the specimen is able to support.

At the other extreme, the model with ℓ_e = 1.0 mm shows α = 0.398, which leads to a value of ε_i close to zero. This could lead to a significant softening process prior to the achievement of the ultimate strength. In this case, the length of the cohesive zone of the material becomes artificially increased, leading to a larger value of force supported by the specimen.

In accordance with these results, it is recommended to avoid values of α below 0.5 in the fiber-related mechanisms to prevent premature softening in the material. The issues observed with the largest element size are geometrical ones not directly related to the application of the solution. The application up to the upper limit ($\alpha = 2$) should be valid.

4.2. Compact Tension

As a second example to showcase the application of the proposed solution, in this section, a Compact Tension test is modeled. Numerical models using two different mesh refinements in the damage zone (i.e., ℓ_e = 1.4 mm and ℓ_e = 3 mm) are solved in two separate sets of simulations: in the first set, the proposed solution is computed for the elements with the smaller size (ℓ_e = 1.4 mm), and the resulting strain parameters are introduced in both models with different mesh refinement. In this way, the influence of the size of the damaged elements on the global response using the same material card can be assessed.

In the second set, the same mesh refinements are used as in the first one, but in this case, the solution is applied considering the size of the elements in the damage zone for each model. In this way, the mesh dependence in the numerical simulations should be reduced, resulting in similar force–displacement responses for both models.

For the validation of the solution by means of Compact Tension tests, the material from component tests is taken as a reference. Initial properties for the elementary ply can be found in Table 3. The stacking sequence for the composite in the Compact Tension test is defined to obtain a quasi-isotropic laminate [0, 45, 90, −45]2s with a ply thickness of

0.262 mm, leading to a total thickness of 4.192 mm. The quasi-isotropic laminate allows for testing the combination of different damage mechanisms in the crack propagation zone.

Table 3. Properties of the composite plies.

Elastic Modulus	E_1	116,700	MPa
	E_2	8800	MPa
Shear Modulus	G_{12}	4670	MPa
Poisson Ratio	ν_{12}	0.26	-
Ultimate Strengths	X_{1T}	1477	MPa
	X_{1C}	708.4	MPa
	X_2	55.4	MPa
	X_6	170	MPa
Fracture Toughness	$\mathcal{G}_{X_{1T}}$	105	N/mm
	$\mathcal{G}_{X_{1C}}$	24	N/mm
	$\mathcal{G}_{X_2}$	0.6	N/mm
	$\mathcal{G}_{X_6}$	8	N/mm

Numerical models are built by stacking the whole laminate into the thickness of one shell element. Material 131 is used to define the laminated material, and the ply definition type 1 is used to define the constitutive behavior of the elementary ply. The meshes used for the numerical models of the Compact Tension test are shown in Figure 9.

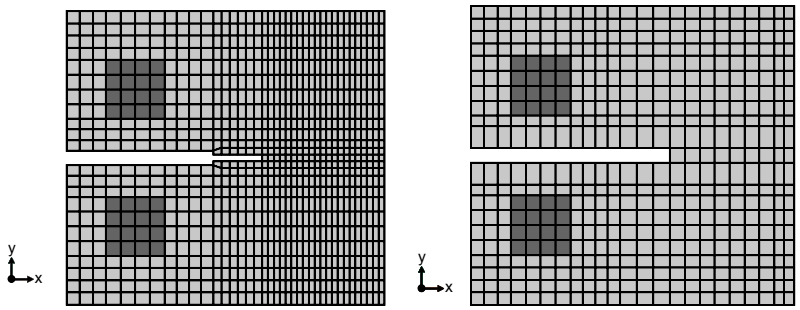


Figure 9. Mesh used in the Compact Tension simulations. Element sizes in the damage zone: (**a**) 1.4 mm, (**b**) 3.0 mm.

4.2.1. Conventional Approach

In the first set of simulations, the same properties are introduced in the material cards for the different mesh refinements. In this case, the influence of the mesh refinement on the numerical results can be assessed.

To determine the strain properties that define the material behavior in Pam-Crash, the factor α must be computed. Considering an element size of $\ell_e = 1.4$ mm and the properties from Table 3, a value of $\alpha \approx 0.25$ is obtained by means of Equation (24). This magnitude for α is below the lower threshold for this factor (0.378). The material cannot be modeled with these properties and the selected size for the finite elements.

Since the objective of this part of the work is to verify that the application of the proposed solution is able to provide strain values that ensure equivalent responses for different mesh refinements, the ultimate strength of the material is increased until valid α values are achieved. The rest of the properties remain unchanged.

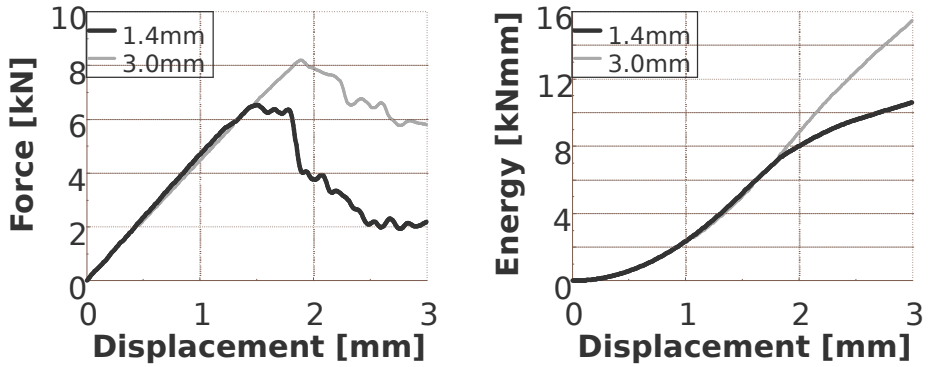
If $\alpha = 0.6$, a hardening behavior that occurs only in the last 10% of the loading phase is obtained. To avoid an excessive increase in the ultimate strength of the material, and

to obtain a constitutive law that shows a small amount of hardening behavior, the factor of $\alpha = 0.6$ is selected. In this way, the hardening process starts at $\sigma_1 = 2066$ MPa, and the ultimate strength of the material is achieved at $\sigma_1 = 2277$ MPa.

Once the value for α is obtained, its application to the curves in Figure 5 yields the β parameters, used to compute the strain parameters that define the constitutive law of the material in Pam-Crash. Thus, for $\alpha_{1.4} = 0.6$, values of $\beta_{i_{1.4}} = 0.9$ and $\beta_{u_{1.4}} = 2.6$ are obtained. The application of the β parameters to Equation (25) results in $\varepsilon^{i}_{1T_{1.4}} = 0.0177$ and $\varepsilon^{u}_{1T_{1.4}} = 0.0509$. A similar process is performed for the other mechanisms in the composite material without modifying the ultimate strength in the matrix-related mechanisms.

To study the dependence of the mesh refinement on the global response of the specimen, the Compact Tension test is simulated using a mesh refinement of $\ell_e = 3$ mm in the damage zone in addition to the simulations performed with $\ell_e = 1.4$ mm.

The same strain values for the description of the constitutive laws are introduced in the material cards to define the behavior of the material in both models. In Figure 10, results from both simulations are shown: For the model with the refined mesh, a good correlation has been obtained. However, when introducing the same properties to define the behavior of the composite ply in the material cards for both mesh refinements, the model with the coarse mesh returns higher values of maximum force and internal energy (i.e., the summation of the internal energy, the energy absorbed by damage and the energy absorbed by the hourglass mode) than the model with the fine mesh.



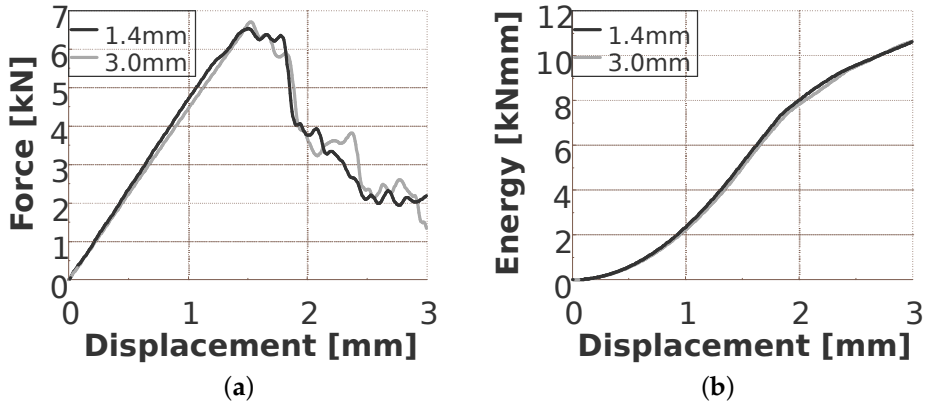
(**a**) (**b**)

Figure 10. Results for a Compact Tension test using the same material definition in different mesh refinements. (**a**) Force–displacement, (**b**) energy–displacement.

4.2.2. Mesh Refinement Consideration

To overcome the dependence of the mesh refinement on the numerical results, the second set of simulations is solved by scaling the material properties to the size of the finite elements in the damage zone through the application of the proposed solution. The material properties adjusted for the last set of simulations are used to define the material properties in this set. Thus, the model with element size $\ell_e = 1.4$ mm retains the definitions for the strain parameters ($\varepsilon^{i}_{1T_{1.4}} = 0.0177$ and $\varepsilon^{u}_{1T_{1.4}} = 0.0509$). For the model with $\ell_e = 3$ mm, the strain parameters are computed taking into account the properties in Table 3 with the adjusted ultimate strength ($\sigma_1 = 2277$ MPa). A value of $\alpha_{3.0} = 1.25$ is obtained, indicating a pure softening law. The application of these parameters to Figure 5 yields $\beta_{i_{3.0}} = 1$ and $\beta_{u_{3.0}} = 1.5$. Finally, an initial strain of $\varepsilon^{i}_{1T_{3.0}} = 0.0194$ and an ultimate strain of $\varepsilon^{u}_{1T_{3.0}} = 0.0292$ are obtained using Equation (25).

Results of this set are shown in Figure 11.



(**a**) (**b**)

Figure 11. Results for a Compact Tension test with the material properties modified by the presented solution. (**a**) Force–displacement, (**b**) energy–displacement.

In this case, both models return a similar description of the force–displacement relationship for the Compact Tension test as well as the same amount of energy dissipated by the damage process. Since the element length of ℓ_e= 1.4 mm is outside the scope of the automotive industry, and element sizes around ℓ_e = 3 mm show suitable values of α, the solution is considered a candidate for the simulation of components under automotive conditions.

4.3. Low-Velocity Impact of Composite Cylinders

The solution presented in Section 3.2.2 is applied herein for the simulation of low-velocity impacts on cylindrical-shaped composite structures with two distinct configurations.

4.3.1. Material and Structure

The cylindrical-shaped structures were manufactured using a unidirectional carbon/epoxy composite material supplied by Hexcel(R). The carbon fibers and matrix used are G1157 (270 gsm) and HexFlow RTM6 epoxy, respectively. The tape is supplied with epoxy binder on both sides (the binder represents approximately 5% of the total tape weight).

Table 3 summarizes the properties of the elementary plies, whilst Table 4 lists the properties for modeling the interfaces between them. These latter properties are introduced in the models in this section to enable simulations to predict potential delamination between plies. All parameters listed were obtained from experimental coupon tests.

Table 4. Material properties of the interfaces between plies.

Elastic Modulus	E	8800	MPa
Shear Modulus	G	4670	MPa
Poisson Ratio	ν	0.45	-
Mode I	τ_3^o	55	MPa
Mode II	τ_{sh}^o	93.7	MPa
Mode I	$\mathcal{G}_{I_c}$	0.637	N/mm
Mode II	$\mathcal{G}_{II_c}$	1.819	N/mm
Coupling Factor	η	3	-

The composite structures in this section are manufactured with a diameter of 500 mm and a total length of 815 mm. Two distinct stacking configurations were considered:

- D01: $[0, 90_2, 0, 45, 0_2, 45, 0, 90, 0_2]$;
- D02: $[0_2, 90, 0_4, 90, 0_4, 90, 0_2]$.

They were manufactured using a Resin Transfer Molding (RTM) process with an external mold to achieve an outer diameter of 50 mm. A Rohacell 71WF inner foam core was used to control laminate thickness. For the D01 specimen, laminate thickness was set to 5 mm, resulting in a ply thickness of 0.416 mm. Specimen D02 had a laminate thickness of 3.93 mm, resulting in a ply thickness of 0.262 mm. A homogeneous distribution of the layers throughout the laminate thickness is assumed for the numerical models.

4.3.2. Experimental Set-Up

Specimens were tested under transverse low-velocity impact loading. The impactor was a cylinder with the same radius as the specimens and a mass of 9.6 kg. It was set to a velocity of 4.56 m/s to achieve an impact energy of 100 J. Specimens were clamped at their extremities to restrict all degrees of freedom except the longitudinal one. In this configuration, the cylinder acts in a flexural mode, minimizing the potential axial forces. Figure 12 shows the experimental set-up. Test conditions and boundaries were selected to be representative of the material requirements in an automotive crash test.

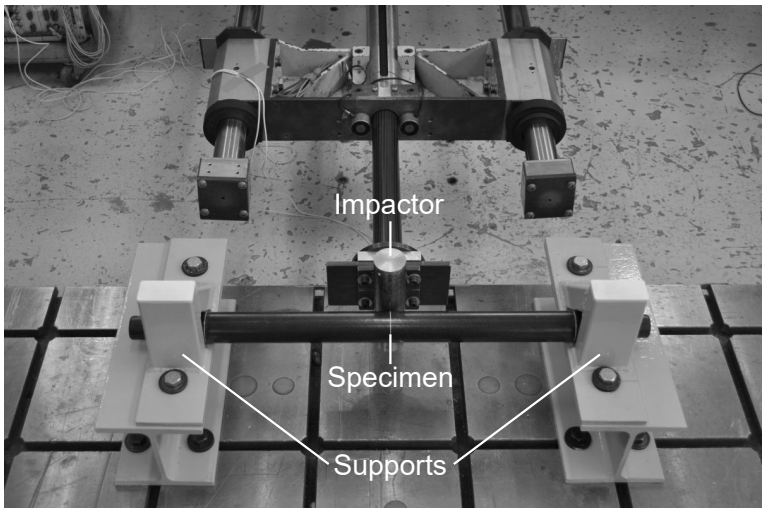


Figure 12. Set-up for low-velocity impact test on the cylinders.

4.3.3. Numerical Models

The composite plies are modeled individually, using one layer of shell elements for each ply in the laminate. Material 131 from the Pam-Crash libraries is applied, and PMT-1 is selected to implement the Ladevèze and Le Dantec [13] constitutive model in Pam-Crash. The proposed solution is applied to define the constitutive behavior for the fiber-related mechanisms. To comply with automotive industry procedures, the mesh comprises square elements with a side length of approximately 5 mm in the outermost ply. In the inner layers, the size of the elements is reduced proportionally to the radius of the cylinder.

To model the behavior of the composite material in Pam-Crash, the mechanical properties of the fiber-related mechanisms must be adapted into their equivalent values of the initial and ultimate strains (ε^{i}_{1I} and ε^{u}_{1I}, respectively). To achieve this and to regularize the energy dissipated by the fiber-related mechanisms, the proposed solution for modeling the damage and failure of composites in Pam-Crash is applied. As the variation in the size of the shell elements is small, the average size of the elements in the failure zone is selected to ensure the validity of a unique ply definition for the entire model. Accordingly, the average size of the elements in specimen D01 is $\overline{\ell}_{e\mathrm{D01}} = 4.265$ mm, whilst for specimen D02, $\overline{\ell}_{e\mathrm{D02}} = 4.5$ mm. Applying these values for element length and material properties from Table 3 in Equation (24) results in the following values for the α parameters: $\alpha_{\mathrm{D01T}} = 0.759$, $\alpha_{\mathrm{D01C}} = 0.764$, $\alpha_{\mathrm{D02T}} = 0.800$ and $\alpha_{\mathrm{D02C}} = 0.805$ (T denotes tension and C denotes compression). The magnitudes obtained indicate that the material is suitable to be modeled

using the selected size for the finite elements in the mesh and that they will behave in a hardening–softening regime (See Figure 5).

To define the matrix-related damage mechanisms, the energy dissipated during their evolution is adjusted using the size of the finite elements in the mesh. Using the element lengths presented above and current material properties, both the transverse and shear mechanisms snap back into their constitutive relation. To obtain a proper description of the matrix-related behavior, a reduction in the ultimate strength is performed until $\alpha = 2$ is reached whilst maintaining the dissipated energy after being scaled to the size of the elements [37]. When this methodology is applied to coupon tests, a small loss of precision in the peak force is compensated by a good description of the energy dissipation.

The interfaces between the adjacent plies in the composite laminate are defined by "tie" elements, using Pam-Crash library material 303. This formulation corresponds to materials that show a degradation profile without a hardening behavior, such as in composite interfaces. In this work, the tie elements are removed from the simulation once they become fully damaged when $d_{tie} = 1$. The associated properties are listed in Table 4. The following properties are required: elastic (E) and shear (G) moduli and Poisson's ratio (ν) are used for the definition of the elastic behavior in the material. The ultimate strength and fracture toughness for the normal ($\tau^o 3, \mathcal{G}I_c$, respectively) and for the shear ($\tau^o sh, \mathcal{G}II_c$, respectively) directions are used for the definition of the constitutive laws in the principal modes of delamination. Finally, a coupling factor (η) is required for the definition of delamination when it occurs in a mixed mode, between normal and shear. These parameters are extracted from delamination tests: double cantilever beam test for the normal-mode related parameters, C-ELS test for the shear-mode related parameters and mixed-mode bending tests for the determination of the η parameter.

The fixtures and the impactor are modeled as rigid bodies to maintain a low computational cost. For their geometric description, a null material type 100 has been selected from the Pam-Crash libraries. The external surfaces of these parts are modeled using shell-type elements, with a size of 0.5 mm, to ensure sufficient precision in the contact algorithm. A rigid body definition type 1 is assigned to make them undeformable. The mass of the impactor is adjusted by means of the thickness of the shell elements and the density of the null material. An initial velocity is imposed on the center of gravity of the impactor, and the remaining degrees of freedom are restricted to reproduce the test conditions.

In numerical simulations where a coarse mesh is modeled, these contact definitions can be insufficient, leading to interpenetration problems (i.e., when a sharp edge in the master surface comes into contact with the center of an element in the slave surface). To avoid this, the contact definition type 43 "edge-to-edge contact" is used to reinforce the description of the interaction between the specimen and the rigid bodies in the model, and the contact type 46 "edge-to-edge self-impacting contact" is used to reinforce the interaction between the different layers of the composite ply.

To define the interactions between the different parts in the numerical models, some contact definitions are added: global contact definition type 36 "self-impacting node to segment with edge treatment" is used to ensure contact between the different layers in the composite laminate, once the tie elements that link them have been eliminated due to delamination damage and the contact definition type 34 "non-symmetric node to segment with edge treatment" is used to model the interactions between the specimen and the parts modeled as rigid bodies.

The foam in the core of the cylinders is modeled using solid type 2 elements corresponding to a "crushable foam for solid elements and SPH". Figure 13 shows the mesh used in the numerical models for simulating the impact event on cylinders.

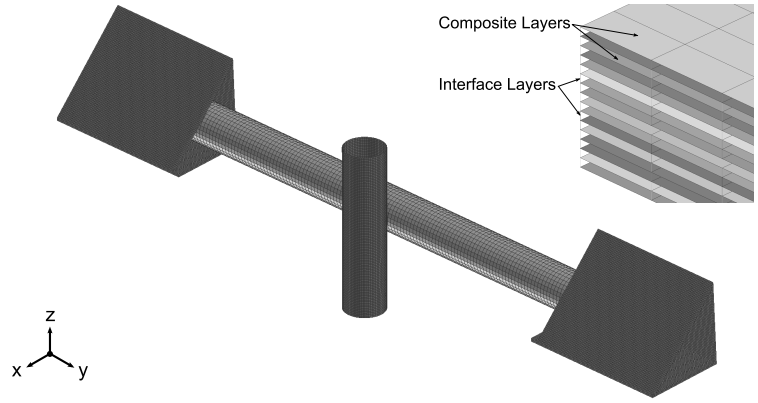
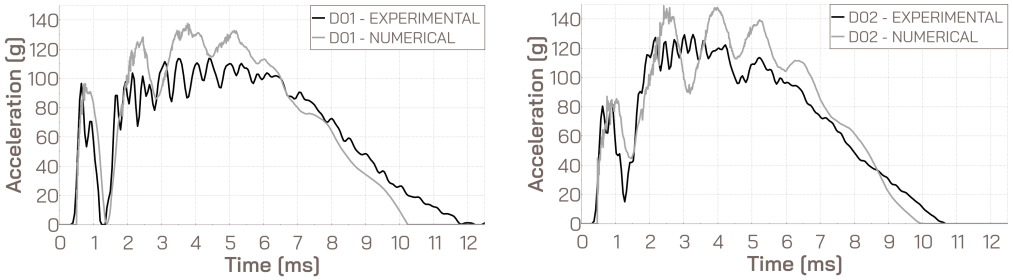


Figure 13. Numerical mesh for simulating of the cylinder under transverse low-velocity impact test.

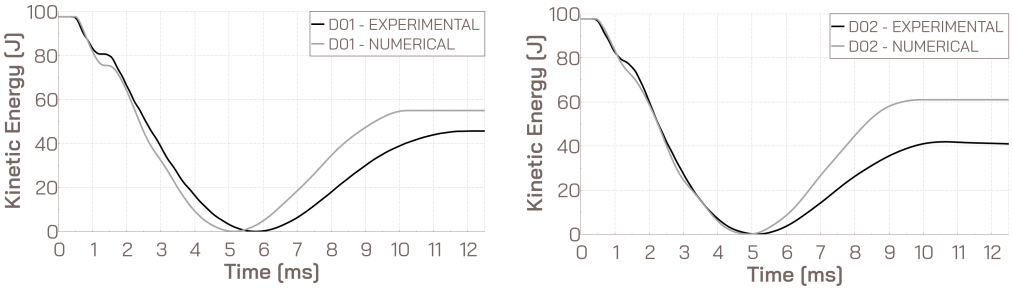
4.3.4. Numerical Results

The correlation between experimental and numerical results is shown in Figures 14–16. In general, good agreement is obtained for both stacking sequences.



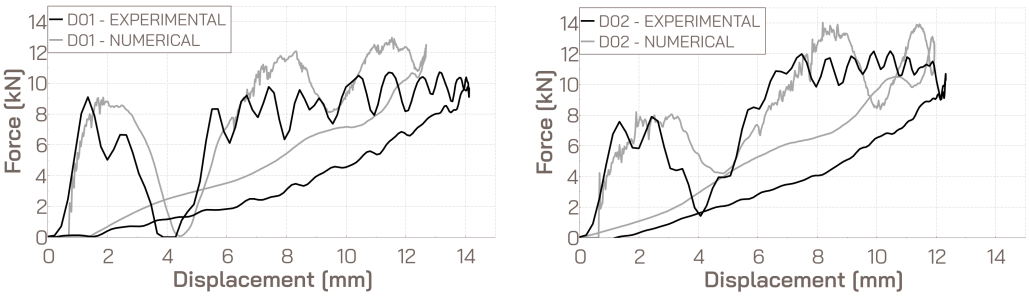
(**a**) (**b**)

Figure 14. Acceleration–time response of the demonstrators: (**a**) specimen D01, (**b**) specimen D02.



(**a**) (**b**)

Figure 15. Displacement–time response of the demonstrators: (**a**) specimen D01, (**b**) specimen D02.



(**a**) (**b**)

Figure 16. Force–displacement response of the demonstrators: (**a**) specimen D01, (**b**) specimen D02.

In the acceleration–time evolution (Figure 14), both cases show good detection of the first peak and mean acceleration. In specimen D01, the acceleration during the crushing process is overestimated, causing the numerical impact total time to be approximately 1.5 ms shorter than the experimental one. The numerical model of specimen D02 provides a good description of the loading phase after the first drop in acceleration until the onset of the crushing process, where the maximum acceleration at this point shows similar magnitudes to the experimental test. After this, a small divergence appears between the numerical and experimental results due to numerical oscillations. Finally, a closer description of the unloading phase is obtained from time $t = 5$ ms until the end of the analysis.

The energy–time results (Figure 15) show good agreement in the loading phase, especially for specimen D02. In D01, equivalent responses are still obtained, but the numerical simulation reaches the returning point 0.6 ms earlier than the experimental results, representing an 11% error (where kinetic energy reaches its minimum at 0 J). After the returning point, both numerical models show faster recovery and thus higher final kinetic energy than the experimental results.

In the force–displacement results, it can be seen how the overestimation of force in the crushing process leads to differences of 10% in the maximum impact displacement for D01, whilst the error in maximum displacement for D02 is smaller with a 3% difference observed compared to the experimental result.

Oscillating behavior can be observed in both the experimental and numerical results, with the experimental results showing a higher frequency, which may have been produced by the sensors on the testing equipment. The numerical results, on the other hand, show a lower frequency, which may have been produced by the FE discretization level.

Correlations show better results for specimen D02. The main reason for this seems to be the specimen configuration, where a higher number of composite layers is found, and more of these layers are oriented at 0°. In specimen D01, there is a higher influence of effects that are not inherent to the composite ply (contacts and interfaces between layers, etc.), which could have led to this increase in force returned by the specimen.

In both cases, the energy dissipation until the returning point shows good correlation, and maximum displacement differences occur in small magnitude. Considering these results, the Pam-Crash constitutive model with the proposed solution reproduces the behavior of the composite structure with sufficient precision for the development of full-vehicle safety performance, where behavior after the returning point is considered as post-test and thus not evaluated in the analysis of results.

Full-vehicle models with the consideration of occupants and airbags require coarse discretization levels for achieving results in acceptable simulation times (element length above 4 mm). Accounting for this, and considering that dimensions in full-vehicle structures are in the order of meters, the precision obtained in maximum displacement (1.44 mm differences in the worst case, D01) is sufficient to allow proper safety-related development in the automotive industry.

Due to the cylindrical shape of the specimens, in the specimen with the most layers, a range of 4 to 5 mm element length was modeled with a single definition of target length for α simulations equal to 4.5 mm. Within these boundaries, a proper correlation level is obtained. It is recommended not to exceed a 25% deviation over the target element length to avoid large deviations in the material's fracture toughness (different material definitions with different element target lengths should be used for elements outside these ranges).

Figure 17 shows the experimental damage that can be observed in the specimens after testing. After the experimental tests, both cylinders showed localized damage in the impact zone, but no damage is observed in the rest of the specimen. In specimen D01, the damaged area forms a round stamp at the point of impact, which seems to be predominant in the matrix phase of the composite material, but fiber damage is not visible. Specimen D02, however, shows a transverse crack in the outer layer, in which it can be seen that the fibers in the first ply are damaged. In D01, the plies are thicker, and several matrix cracks are present in the impacted region.

Since in Pam-Crash the fiber damage variable is not available to be plotted, the total damage variable for some selected layers is plotted in Figure 17. In the outer plies (ply 1), both models show damage distribution. In D01, the damage zone occupies a larger area than in D02, where it is more localized on the line of impact. Despite the coarse mesh refinement and the lack of more precise damage variables, it can be seen that simulations trend toward the damage observed in the experimental tests, where D01 showed a widespread damage distribution and D02 a crack in the impact zone. In the innermost layers, both models exhibit damage distribution around the impact point. D02 shows a greater area and magnitude in this case: although visual inspection exhibited a clean crack in the outer layer, damage seems to become more critical in the inner layers than for the D01 configuration.

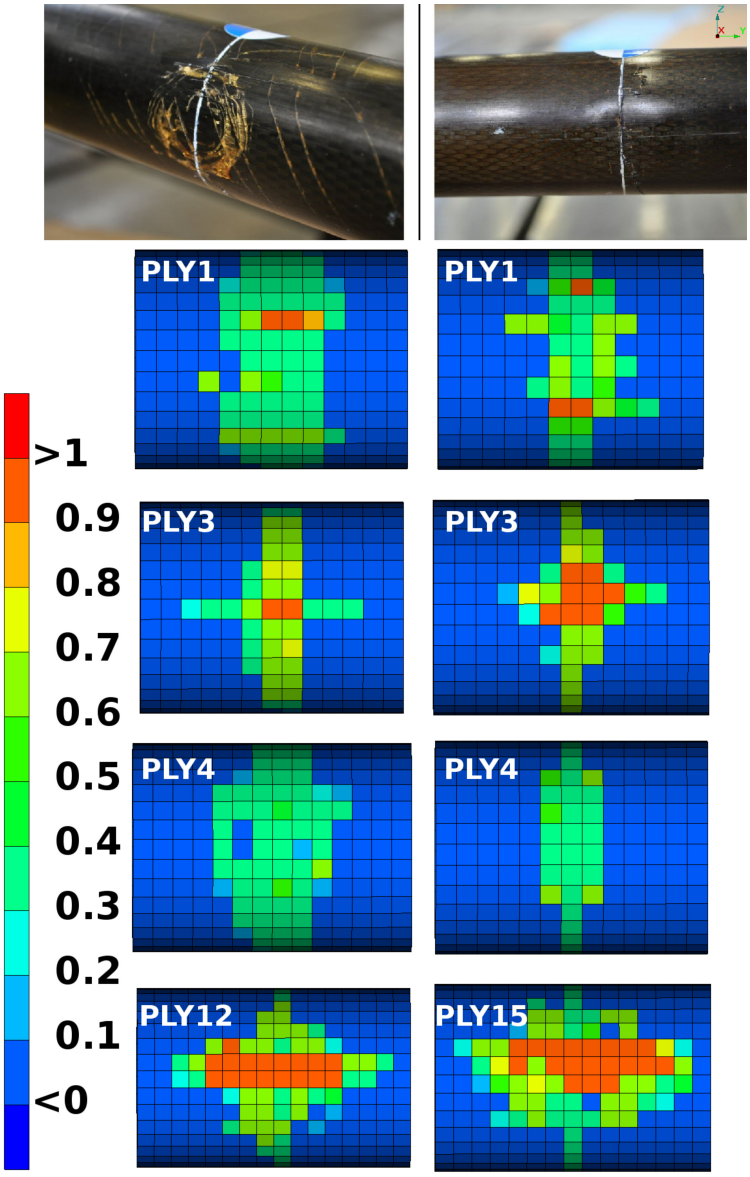


Figure 17. Damage description after the experimental tests and numerical simulations. D01 (**left**), D02 (**right**).

The principal motivation that led to the development of the solution presented here was to simulate large composite structures in a reasonably short computational time whilst maintaining mesh objectivity of the response. Table 5 shows the computational data gathered during the simulation of the specimens. When FE simulation is solved in an

explicit mode, the most important factor that governs the time to compute the numerical solution is the stable time increment, as the magnitude of this property will set the number of steps that the simulation must perform until it is finished. The main parameters used to determine the stable time increment are the density and elastic modulus of the involved materials and the size of the finite elements present in the simulation. As can be seen in Table 5, the stable time increment is smaller for specimen D02 than for specimen D01. Since the material properties are the same for both numerical models, the factor that can cause this difference is the size of the tie elements used to model the interfaces between layers. Because specimen D02 comprises a larger number of layers and a smaller laminate thickness, its tie elements are shorter than those of D01, and the stable time increment is influenced by this. Even with the smaller time increment and the larger number of elements, a similar simulation time is observed. As such, in simulations performed with 8 CPU parallelization, the impact test on specimen D01 is computed in 2.3 h, whilst simulations for the impact of specimen D02 last about 2.16 h. A target time of 0.5 μs was set in the models, and a general mass scaling was applied, which only takes effect in nodes below the target stable time increment. In this case, the tied nodes in the zone of reduced radius in the specimen were the ones where mass scaling was introduced. Mass scaling is limited to a 1% increase so as not to influence the dynamics of the materials in the simulations.

Table 5. Computational results for the numerical models of the specimens.

Specimen	D01	D02
CPUs	8	8
Stable time increment (ms)	6.789×10^{-5}	5.734×10^{-5}
CPU time (h)	2.3	2.16
Composite mass (kg)	1.5310	1.75555
Foam mass (kg)	0.0453	0.0514
Mass increase (%)	0.94	1.06
Mass increase (kg)	0.145	0.1654

5. Conclusions

In this work, an engineering solution for modeling the damage and failure of unidirectional-reinforced composite materials with Pam-Crash is proposed. For better understanding, a description of the available constitutive model is provided and the main difficulties related to its application are explained. The proposed solution allows the use of material properties and employs the crack band methodology to ensure proper energy dissipation by crack propagation, considering the size of the finite elements. It then includes a study for the viability of modeling the composite material in the selected element. Finally, it provides the strain-related inputs to be introduced in the material card to ensure behavior in accordance with the desired material properties. When applied in the simulation of Open Hole and Compact Tension tests, the solution results in a proper method for dealing with the dependency of the numerical response on mesh refinement. After checking the application of the proposed solution over coupon tests, it is then applied to the simulation of low-velocity impact tests over large composite cylinders. Two configurations were tested experimentally, and their numerical simulations resulted in good correlation for the acceleration evolution in both cases. In the description of the global damage variable for the shell elements, both simulations show similar damage patterns as in experimental tests. Computational data have been gathered from the simulation of the cylinders, resulting in a computational time for the solution of about 2.15 h, which is a short time for simulations of impact tests on large structures, especially when composite materials are involved. Considering the quality of the component correlation and the computational time for its achievement, the solution becomes of interest for application in the development of components and structures for safety-related applications in the automotive industry.

Author Contributions: Conceptualization, E.M.-S. and P.C.; methodology, E.M.-S. and P.C.; validation, E.M.-S., P.C. and L.G.B.; formal analysis, E.M.-S.; investigation, E.M.-S.; resources, P.C.; writing—original draft preparation, E.M.-S.; writing—review and editing, P.C. and L.G.B.; supervision, L.G.B.; project administration, P.C.; funding acquisition, P.C. All authors have read and agreed to the published version of the manuscript.

Funding: This work has been supported by the Spanish State Research Agency AEI through the project PID2022-139903OA-I00 (Blast_IT) and by the European Union's research and innovation program through project BIOntier, grant agreement 101155925. Lucia Gratiela Barbu is a Serra Húnter Fellow. The authors gratefully acknowledge the support.

Data Availability Statement: Data available on request due to restrictions.

Acknowledgments: Experimental data shown in this work are extracted from the project "Demostrador de un grid para actividades de simulación con requisitos extermos de cálculo", which was funded by European Regional Development Funds (ERDF) through the Centro para el Desarrollo Tecnológico Industrial (CDTI) of the Spanish Government (Ministerio de Economía y Competitividad).

Conflicts of Interest: All the authors declare that the research was conducted in the absence of any commercial or financial relationships that could be construed as a potential conflict of interest.

References

1. Kim, D.H.; Choi, D.H.; Kim, H.S. Design optimization of a carbon fiber reinforced composite automotive lower arm. *Compos. Part B Eng.* **2014**, *58*, 400–407. [CrossRef]
2. Talib, A.R.A.; Ali, A.; Goudah, G.; Lah, N.A.C.; Golestaneh, A. Developing a composite based elliptic spring for automotive applications. *Materials & Design* **2010**, *31*, 475–484.
3. Gong, Y.; Yang, Z.G. Fracture failure analysis of automotive accelerator pedal arms with polymer matrix composite material. *Compos. Part B Eng.* **2013**, *53*, 103–111. [CrossRef]
4. Lim, T.S.; Lee, D.G. Mechanically fastened composite side-door impact beams for passenger cars designed for shear-out failure modes. *Compos. Struct.* **2002**, *56*, 211–221. [CrossRef]
5. Durrenberger, L.; Lemoine, X.; Molinari, A. Effects of pre-strain and bake-hardening on the crash properties of a top-hat section. *J. Mater. Process. Technol.* **2011**, *211*, 1937–1947. [CrossRef]
6. Lanzi, L.; Bisagni, C.; Ricci, S. Neural network systems to reproduce crash behavior of structural components. *Comput. Struct.* **2004**, *82*, 93–108. [CrossRef]
7. Bisagni, C. Crashworthiness of helicopter subfloor structures. *Int. J. Impact Eng.* **2002**, *27*, 1067–1082. [CrossRef]
8. Mei, L.; Thole, C. Data analysis for parallel car-crash simulation results and model optimization. *Simul. Model. Pract. Theory* **2008**, *16*, 329–337. [CrossRef]
9. Pickett, A.K.; Pyttel, T.; Payen, F.; Lauro, F.; Petrinic, N.; Werner, H.; Christlein, J. Failure prediction for advanced crashworthiness of transportation vehicles. *Int. J. Impact Eng.* **2004**, *30*, 853–872. [CrossRef]
10. Zarei, H.; Kröger, M.; Albertsen, H. An experimental and numerical crashworthiness investigation of thermoplastic composite crash boxes. *Compos. Struct.* **2008**, *85*, 245–257. [CrossRef]
11. Matzenmiller, A.; Lubliner, J.; Taylor, R. A constitutive model for anisotropic damage in fiber-composites. *Mech. Mater.* **1995**, *20*, 125–152. [CrossRef]
12. Maimí, P.; Camanho, P.P.; Mayugo, J.A.; Dávila, C.G. A continuum damage model for composite laminates: Part I: Constitutive model. *Mech. Mater.* **2007**, *39*, 897–908. [CrossRef]
13. Ladevèze, P.; Le Dantec, E. Damage modelling of the elementary ply for laminated composites. *Compos. Sci. Technol.* **1992**, *43*, 257–267. [CrossRef]
14. Engineering Systems International. *PAM-CRASH Solver Reference Manual*; Engineering Systems International: Rungis, France, 2022.
15. Bažant, Z.P.; Planas, J. *Fracture and Size Effect in Concrete and Other Quasibrittle Materials*; CRC Press: Boca Ratón, FL, USA, 1998.
16. Pan, F.; Zhu, P.; Zhang, Y. Metamodel-based lightweight design of B-pillar with {TWB} structure via support vector regression. *Comput. Struct.* **2010**, *88*, 36–44. [CrossRef]
17. Golman, A.J.; Danelson, K.A.; Miller, L.E.; Stitzel, J.D. Injury prediction in a side impact crash using human body model simulation. *Accid. Anal. Prev.* **2014**, *64*, 1–8. [CrossRef]
18. Kang, K.T.; Chun, H.J.; Park, J.C.; Na, W.J.; Hong, H.T.; Hwang, I.H. Design of a composite roll bar for the improvement of bus rollover crashworthiness. *Compos. Part B Eng.* **2012**, *43*, 1705–1713. [CrossRef]
19. Engineering Systems International. *PAM-CRASH Users Manuals*; Engineering Systems International: Rungis, France, 2012.
20. Hurez, A. Modélisation du Comportement de Stratifiés avec prise en compte de L'évolution de L'endommagement à L'aide D'un Elément de Plaque Incluant les Effets du Cisaillement Transversal. Ph.D. Thesis, Univesité de Technologie de Compiègne, Compiègne, France, 1993.

21. Greve, L.; Pickett, A. Modelling damage and failure in carbon/epoxy non-crimp fabric composites including effects of fabric pre-shear. *Compos. Part A Appl. Sci. Manuf.* **2006**, *37*, 1983–2001. [CrossRef]
22. O'Higgins, R.; McCarthy, M. *Damage Modelling of Fibre Reinforced Polymer Matrix Composite Open Hole Tension Specimens Using the Ladevèze Damage Model in Pam-CRASH*; Technical Report November; University of Limerick: Limerick, Ireland, 2016.
23. Elices, M.; Guinea, G.; Gómez, J.; Planas, J. The cohesive zone model: Advantages, limitations and challenges. *Eng. Fract. Mech.* **2002**, *69*, 137–163. [CrossRef]
24. Barbu, L.G.; Oller, S.; Martinez, X.; Barbat, A.H. High-cycle fatigue constitutive model and a load-advance strategy for the analysis of unidirectional fiber reinforced composites subjected to longitudinal loads. *Compos. Struct.* **2019**, *220*, 622–641. [CrossRef]
25. Taherzadeh-Fard, A.; Cornejo, A.; Jiménez, S.; Barbu, L.G. A rule of mixtures approach for delamination damage analysis in composite materials. *Compos. Sci. Technol.* **2023**, *242*, 110160. [CrossRef]
26. Gonçalves, L.A.; Jiménez, S.; Cornejo, A.; Tedesco, M.M.; Barbu, L.G. A high cycle fatigue numerical framework for component-level virtual fatigue testing: Application to a light-duty vehicle lower control arm. *Eng. Struct.* **2024**, *311*, 118198. [CrossRef]
27. Bažant, Z.P.; Oh, B. Crack Band Theory for Fracture of Concrete. *Matériaux et Constructions* **1983**, *16*, 155–177. [CrossRef]
28. Iannucci, L.; Willows, M.L. An energy based damage mechanics approach to modelling impact onto woven composite materials—Part I: Numerical models. *Compos. Part A Appl. Sci. Manuf.* **2006**, *37*, 2041–2056. [CrossRef]
29. Iannucci, L.; Willows, M.L. An energy based damage mechanics approach to modelling impact onto woven composite materials—Part II. Experimental and numerical results. *Compos. Part A Appl. Sci. Manuf.* **2007**, *38*, 540–554. [CrossRef]
30. Frizzell, R.M.; McCarthy, C.T.; McCarthy, M.A. Predicting the effects of geometry on the behaviour of fibre metal laminate joints. *Compos. Struct.* **2011**, *93*, 1877–1889. [CrossRef]
31. Frizzell, R.M.; McCarthy, C.T.; McCarthy, M.A. Simulating damage and delamination in fibre metal laminate joints using a three-dimensional damage model with cohesive elements and damage regularisation. *Compos. Sci. Technol.* **2011**, *71*, 1225–1235. [CrossRef]
32. Ladevèze, P.; Allix, O.; Deü, J.F.; Lévêque, D. A mesomodel for localisation and damage computation in laminates. *Comput. Methods Appl. Mech. Eng.* **2000**, *183*, 105–122. [CrossRef]
33. Maimí, P.; González, E.V.; Gascons, N.; Ripoll, L.L. Size Effect Law and Critical Distance Theories to Predict the Nominal Strength of Quasibrittle Structures. *Appl. Mech. Rev.* **2013**, *65*, 1–16. [CrossRef]
34. Laffan, M.; Pinho, S.T.; Robinson, P.; McMillan, A.J. Translaminar fracture toughness testing of composites: A review. *Polym. Test.* **2012**, *31*, 481–489. [CrossRef]
35. Ortega, A.; Maimí, P.; González, E.V.; Ripoll, L. Compact tension specimen for orthotropic materials. *Compos. Part A Appl. Sci. Manuf.* **2014**, *63*, 85–93. [CrossRef]
36. Ortega, A.; Maimí, P.; González, E.V.; Trias, D. Characterization of the translaminar fracture cohesive law. *Compos. Part A Appl. Sci. Manuf.* **2016**, *91*, 501–509. [CrossRef]
37. Maimí, P.; Camanho, P.P.; Mayugo, J.A.; Dávila, C.G. A continuum damage model for composite laminates: Part II: Computational implementation and validation. *Mech. Mater.* **2007**, *39*, 909–919. [CrossRef]

Disclaimer/Publisher's Note: The statements, opinions and data contained in all publications are solely those of the individual author(s) and contributor(s) and not of MDPI and/or the editor(s). MDPI and/or the editor(s) disclaim responsibility for any injury to people or property resulting from any ideas, methods, instructions or products referred to in the content.